Research Article | Open Access

Soft Science

Liu *et al. Soft Sci.* **2026**, *6*, 34 **DOI:**10.20517/ss.2025.143

High-performance, noninvasive flexible sensing array for gesture and handwriting recognition assisted by machine learning

Lu Liu[1,2,3,*], Hengxiang Liu[2], Shudan Li[1,3], Xinlu Wei[1,3], Jiantao Yao[1,3], Bo Han[1,3], Hao Zhou[1,3], Dianyu Wang[4], Yundou Xu[1,3,*], Xiaoli Jia[2,*]

Keywords:
Flexible sensor array, handwriting correction, human-machine interaction, gesture recognition, wearable device

Citation: Liu, L.; Liu, H.; Li, S.; Wei, X.; Yao, J.; Han, B.; Zhou, H.; Wang, D.; Xu, Y.; Jia, X. High-performance, noninvasive flexible sensing array for gesture and handwriting recognition assisted by machine learning. *Soft Sci.* **2026**, *6*, 34. https://dx.doi.org/10.20517/ss.2025.143

Received: 19 Dec 2025 **First Decision:** 6 Feb 2026 **Revised:** 7 Apr 2026 **Accepted:** 27 Apr 2026 **Published:** 9 May 2026

Academic Editor: Guanglei Wu
Copy Editor: Pei-Yun Wang
Production Editor: Pei-Yun Wang

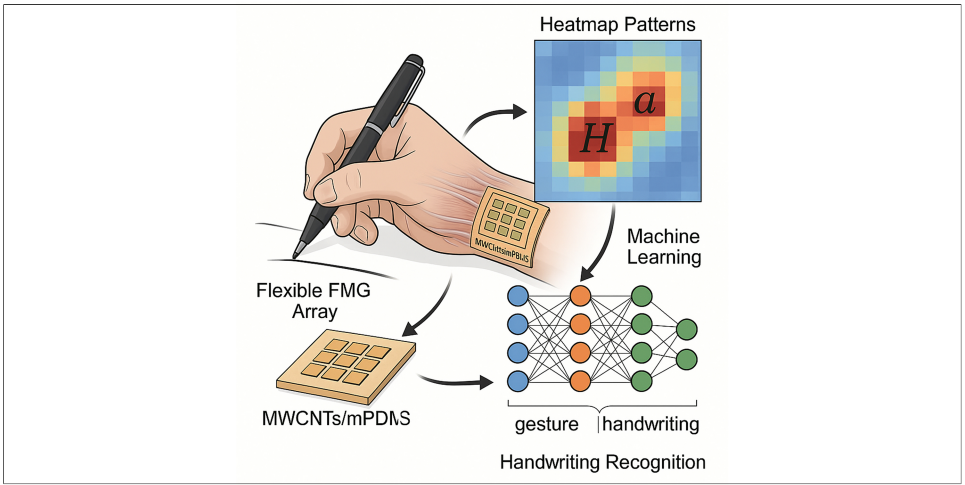

Abstract

Wearable handwriting interfaces represent one of the most challenging frontiers in human–machine interaction as the precise decoding of subtle neuromuscular coordination is required. In this study, a machine-learning-assisted flexible force myography (FMG) array is presented for gesture and handwriting recognition. The system is constructed based on a 3 × 3 microstructured polydimethylsiloxane/multiwalled carbon nanotube array with a mass of 0.15 g and a thickness of 0.43 mm. The system is characterized by its high sensitivity (~1.364 kPa^{-1}), low hysteresis [4.75% full scale (F.S.)], rapid response and recovery times (12 and 16 ms, respectively), and robust mechanical stability under bending, overload, and water-immersion conditions. Compared with conventional surface electromyography or electret-based FMG systems, quantitative mapping of the spatiotemporal deformation of wrist tendons is achieved, enabling the handwriting sequence, stroke count, and continuity to be decoded with an accuracy of 99.54% ± 0.16%.

[1]Parallel Robot and Mechatronic System Laboratory of Hebei Province, Yanshan University, Qinhuangdao 066004, Hebei, China.
[2]College of Mechanical and Transportation Engineering, China University of Petroleum-Beijing, Beijing 102249, China.
[3]Hebei Provincial National Defense Key Discipline Laboratory of General Technology on Military Basic Electromechanical Products, Yanshan University, Qinhuangdao 066004, Hebei, China.
[4]School of Chemical Engineering, Zhengzhou University, Zhengzhou 450001, Henan, China.

***Correspondence to:** Dr. Lu Liu, Prof. Yundou Xu, Parallel Robot and Mechatronic System Laboratory of Hebei Province, Yanshan University, Qinhuangdao 066004, Hebei, China. E-mail: luliu@ysu.edu.cn; ydxu@ysu.edu.cn; Prof. Xiaoli Jia, College of Mechanical and Transportation Engineering, China University of Petroleum-Beijing, Beijing 102249, China. E-mail: xljia@cup.edu.cn

Mechanistic analysis indicates that pressure modulation patterns are governed by the coordinated activation of the coordinated activation of the flexor carpi radialis, flexor digitorum superficialis, and flexor digitorum profundus, and the flexor carpi ulnaris–flexor digitorum profundus groups, thereby providing a physiological basis for character-specific responses. This work extends FMG sensing from gesture-level motion capture to fine-grained handwriting interpretation, and a compact, noninvasive, and scalable platform is established for wearable handwriting recognition and human–machine interaction.

INTRODUCTION

Human handwriting is considered one of the most intricate forms of human–machine interaction, in which fine neuromuscular coordination and continuous force modulation are involved[1-4]. The accurate perception and decoding of these subtle motions through noninvasive wearable systems are essential for next-generation intelligent interfaces, digital healthcare, and neurorehabilitation[5-9]. Unlike coarse gestures, handwriting consists of overlapping micromovements that encode individual motor patterns and cognitive intent, making the continuous and comfortable capture of muscle deformation challenging[10-14].

Over the past decade, noninvasive handwriting recognition has been explored using vision-based systems, surface electromyography (sEMG), and force myography (FMG)[15-19]. Vision-based approaches leveraging deep learning models have achieved recognition accuracies exceeding 99% on benchmark datasets such as the handwriting database developed by the Institute for Artificial Intelligence and Pattern Recognition at the University of Bern, owing to rich spatial and structural information[20-25]. Moreover, such systems often rely on relatively simple hardware, making them suitable for high-precision offline recognition. However, their performance strongly depends on imaging conditions and can be affected by occlusion, illumination variation, and camera alignment. In addition, visual methods do not directly capture underlying muscle activity, which limits their ability to distinguish writing patterns generated by similar trajectories but different biomechanical dynamics[26-29].

sEMG is a widely used alternative method for capturing bioelectric signals associated with muscle activation[30-35]. Recent advances using high-density electrode arrays (> 64 channels) have demonstrated that fine motor patterns can be resolved by sEMG, enabling detailed decoding of complex movements. Nevertheless, sEMG systems require precise electrode placement and stable skin–electrode interfaces, and they are sensitive to sweat, motion artifacts, and intersubject variability, thereby limiting their robustness in long-term wearable applications[36-39].

In parallel, soft and flexible pressure sensors have been rapidly developed, with reported sensitivities exceeding 1 kPa^{-1}, detection limits of a few pascals, response times within tens of milliseconds, and significantly reduced hysteresis[40-43]. These advances are primarily attributed to structural engineering strategies, including porous and hierarchical microarchitectures, as well as percolating nanocomposite conductive networks that amplify contact and tunneling effects under deformation[44-47]. In addition, standalone flexible and stretchable device platforms have been developed to ensure conformal contact and mechanical robustness under repeated bending and stretching, which is essential for wearable sensing applications[48-50].

Despite these substantial advances at the material and device levels, a fundamental challenge remains in translating high-performance sensing into reliable system-level signal acquisition under dynamic and unconstrained conditions. In particular, maintaining a balance between sensitivity, linear detection range, and long-term stability is difficult when sensors are subjected to complex, multi-axis deformation and interfacial variations during real-world use. These limitations become more pronounced in handwriting

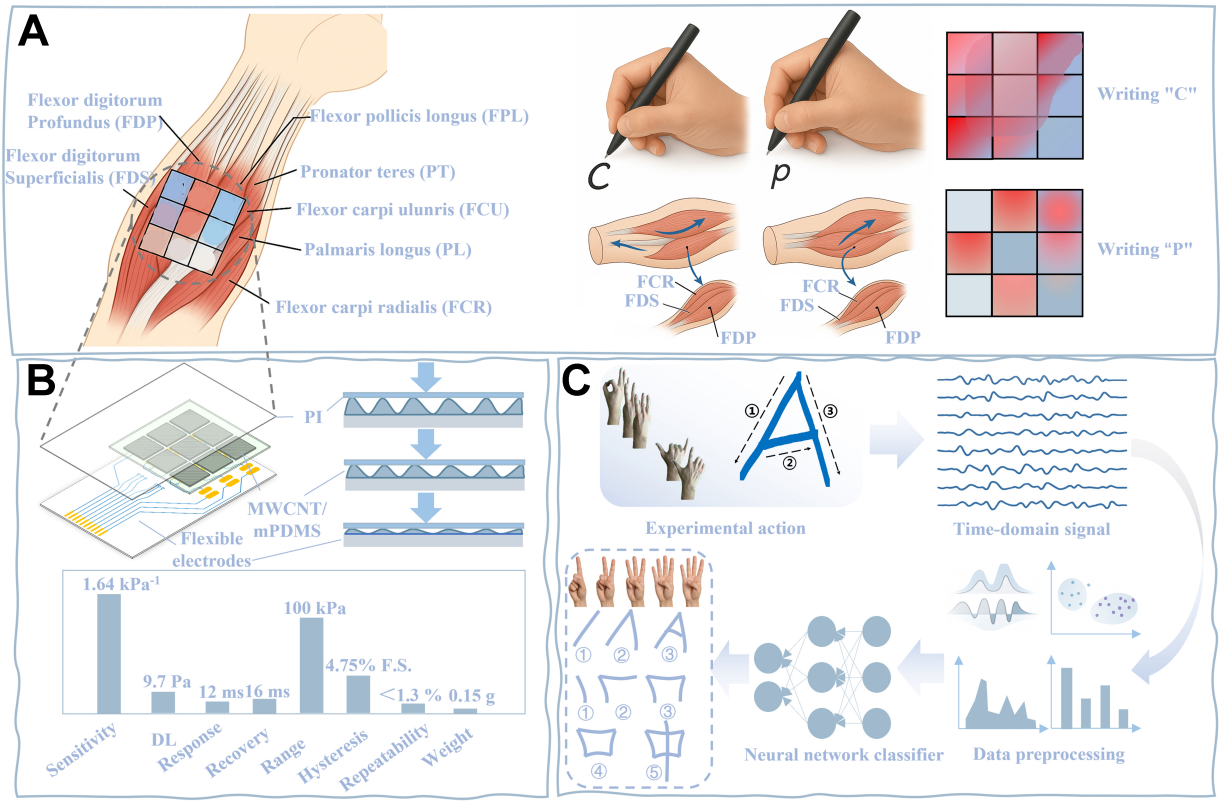

Figure 1. Concept and mechanism of the flexible FMG handwriting recognition system. (A) Schematic of the mechanism response of the medial wrist flexor group and a 3 × 3 flexible array during the writing process; (B) Exploded view and key performance indicators of the flexible pressure sensor array based on MWCNTs/mPDMS; (C) Signal acquisition and neural network decoding process, converting multichannel time waveforms into gesture and handwriting classifications. FMG: Flexible force myography; MWCNTs: multiwalled carbon nanotubes; mPDMS: microstructured polydimethylsiloxane; PI: polyimide; DL: detection limit.

recognition, where subtle, continuous, and overlapping muscle deformations must be accurately captured.

In this context, FMG, which measures pressure variations induced by muscle deformation, is considered to offer a mechanically mediated sensing modality that is inherently robust to electrical impedance fluctuations and exhibits low sensitivity to environmental perturbations. Although FMG provides lower spatial resolution than vision-based systems and high-density sEMG, it allows for stable, low-complexity, and wearable-compatible sensing. Therefore, FMG is regarded as a practical pathway that bridges high-performance flexible sensing and real-world human–machine interaction, particularly for continuous handwriting-recognition tasks that require both robustness and user comfort.

In this study, we report a machine-learning-assisted flexible FMG array that overcomes these limitations through a multiwalled carbon nanotube/microstructured polydimethylsiloxane (MWCNT/mPDMS) composite integrated with a lightweight neural decoding model [Figure 1]. As illustrated in Figure 1, distinct handwriting motions generate distinguishable pressure distribution patterns in the forearm tissues, which are captured by the FMG sensor array. The pressure patterns underlying the differential sensing behavior are further analyzed in Supplementary Note 1, where representative forearm anatomical structures are provided to explain the observed handwriting-related pressure variations. The nine-channel array (0.15 g, 0.43 mm thick) is conformally attached to the wrist surface and demonstrates a sensitivity of approximately 1.364 kPa^{-1} within 0-100 kPa, a detection limit of 9.74 Pa, and response and recovery times of 12 and 16 ms, respectively. It shows linearity and repeatability (< 2.6% and 1.3%, respectively), low hysteresis [4.75% full scale (F.S.)], and a stable performance under a 1.3 MPa overload and 3,000 loading cycles.

By decoding spatiotemporal pressure maps through a neural network trained on hybrid amplitude–frequency features, accuracies of 99.54% ± 0.16% for handwriting recognition and 97% for complex gesture recognition are achieved without recalibration. Beyond sensitivity and precision, the array shows robustness against bending, water exposure, and repeated attachment. Systematic benchmarking against representative sEMG and FMG systems demonstrates the improved accuracy, mechanical reliability, and cross-user generalization of this system. The platform can recognize continuous and style-variable handwriting without explicit segmentation or user-dependent calibration, thereby addressing a long-standing limitation of noninvasive interfaces.

In summary, this work presents a high-performance, lightweight, and robust FMG-based flexible sensing array that bridges gesture-level sensing and handwriting decoding. Through microstructured material design and machine-learning-driven analysis, the proposed system enables reliable wearable handwriting recognition and provides a scalable framework for intelligent human–machine interfaces and digital authentication.

RESULTS AND DISCUSSION

Fabrication and characterization of flexible sensor arrays for wireless data transmission

The fabrication process of the flexible sensor array is illustrated in Figure 2A. Each sensing unit consists of an mPDMS substrate integrated with an MWCNT conductive layer and flexible electrodes. The mPDMS substrate was fabricated via a replica-molding strategy. A structured mold was first prepared using selective laser sintering (SLS), where nylon powder was selectively fused layer-by-layer under laser irradiation. The polydimethylsiloxane (PDMS) prepolymer and curing agent (Sylgard 184, Dow Corning) were mixed at a mass ratio of 10:1, stirred for 10 min, and then degassed under a vacuum for 30 min. The mixture was cast into the SLS-fabricated mold and cured at 80 °C for 2 h. After cooling, the elastomer was peeled off, thereby replicating the microstructured surface. To promote interfacial adhesion, the mPDMS surface was treated with oxygen plasma for 30-60 s to enhance surface wettability and facilitate subsequent deposition.

MWCNTs were dispersed in ethanol at a concentration of 1 mg/mL, followed by ultrasonication to obtain a homogeneous suspension. A conductive MWCNT network was then deposited onto the mPDMS surface via physical vapor deposition (PVD). The deposition was performed in a vacuum chamber with a base pressure of approximately 5×10^{-3} Pa and a working pressure of approximately 0.5 Pa, while the substrate was maintained at 25 ± 3 °C. The deposition duration was controlled within 5-10 min. Flexible electrodes were fabricated by first depositing copper nanoparticles onto a rigid substrate via drop-casting, after which laser patterning was used to define the electrode geometry. Polyimide (PI) was then cast and thermally cured to form a flexible substrate. After release, the patterned copper layer was embedded onto the PI surface, forming a flexible conductive electrode. Finally, the MWCNT-coated mPDMS layer and the flexible electrode layer were assembled in a face-to-face configuration and encapsulated using a PDMS film, resulting in the fully integrated flexible-pressure-sensor array.

The entire device consisted of a 3 × 3 nine-channel flexible pressure sensor array with a sensing area of approximately 14 × 14 mm. The actual object and size are presented in Supplementary Figures 1 and 2. Notably, the flexible sensor array exhibited an ultralight design, with a mass of 0.15 g and a thickness of 0.43 mm. Supplementary Figure 3A presents scanning electron microscopy (SEM) images of the PDMS surface without SLS treatment at different magnifications. The PDMS surface is shown to be relatively smooth and without a distinct surface structure. Figure 2B shows an SEM image of the mPDMS, wherein the surface observed after SLS treatment exhibited a pronounced microstructured morphology. SEM images of the MWCNT/mPDMS system at different magnifications are presented in Figure 2C and Supplementary Figure 3B. The microstructure remains clearly observable even at a magnification of 10,000×. Figure 2D and

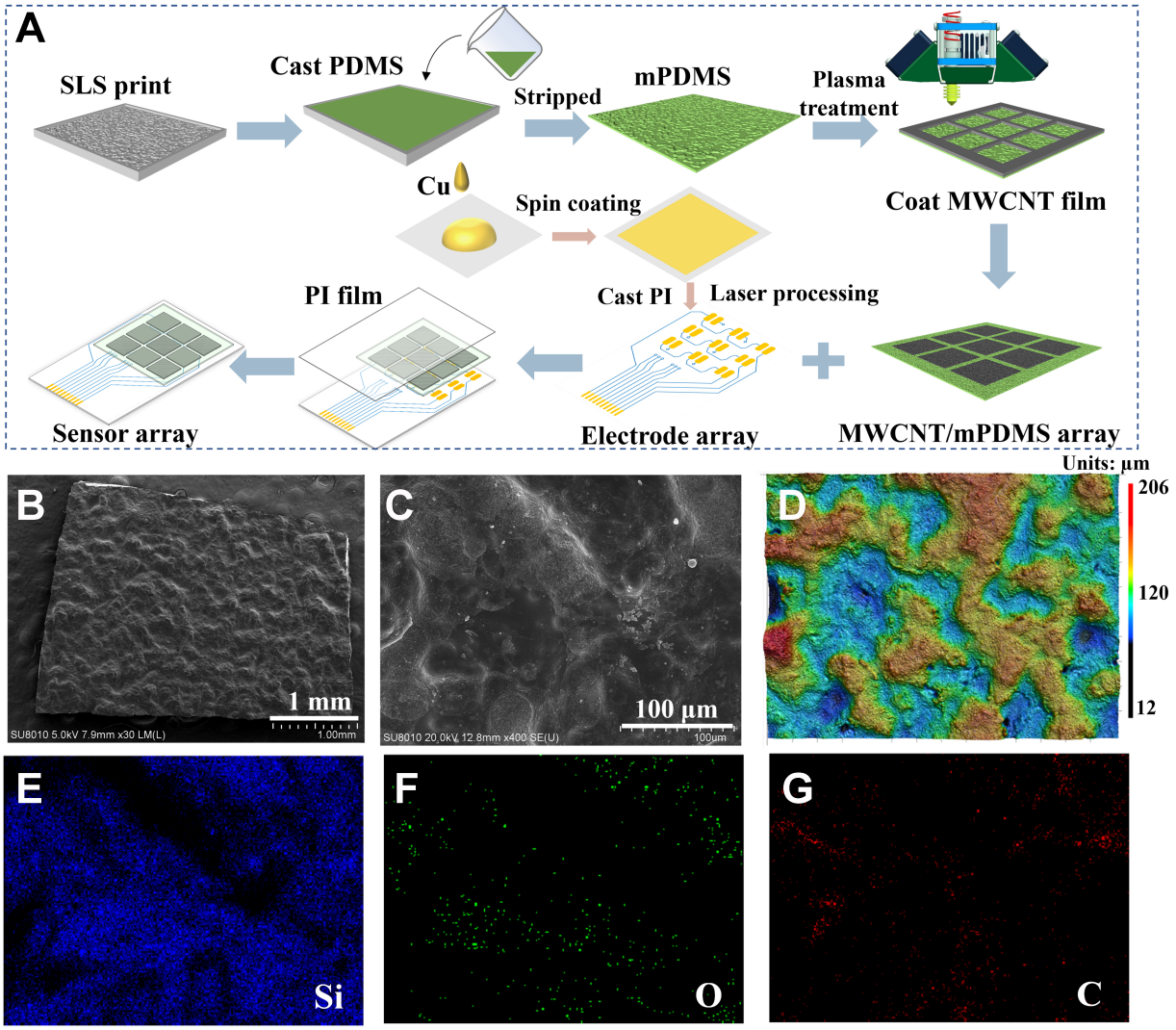

Figure 2. Preparation process and characterization of the flexible pressure sensor array. (A) Preparation process of the flexible sensor array. SEM images of (B) mPDMS and (C) MWCNTs/PDMS; (D) 3D topography scanning image of the MWCNT/mPDMS surface; (E-G) Elemental distribution of MWCNT/mPDMS. SEM: Scanning electron microscopy; mPDMS: microstructured polydimethylsiloxane; MWCNTs: multiwalled carbon nanotubes; SLS: selective laser sintering; PI: polyimide.

Supplementary Figure 4 show three-dimensional topography images of the PDMS and MWCNTs/mPDMS surfaces, and the surface line-scan roughness information is provided in Supplementary Figure 5. The PDMS surface exhibited a small height fluctuation with a roughness of only 0.765 μm, suggesting a relatively smooth surface with minimal topographical variation. By contrast, the MWCNT/mPDMS surface exhibited significant height variation, with a maximum height difference of approximately 65 μm and a surface roughness of 14.32 μm. These characterization results confirm the successful fabrication of a PDMS film with a surface microstructure via SLS. SEM and three-dimensional surface profilometry analyses were employed to elucidate the structural characteristics introduced by SLS. The precise replication of the designed microstructures on the PDMS surface was confirmed, and their effect on the sensing performance was investigated. The mPDMS layer exhibited a significantly higher surface roughness (Ra ≈ 14.32 μm) compared with the pristine PDMS film (Ra ≈ 0.76 μm), indicating an enlarged effective contact area and enhanced interfacial friction at the electrode–polymer interface under compression. This roughened morphology facilitates the formation of multiple tunneling pathways among the embedded MWCNTs, thereby improving the pressure-dependent conductance response. By contrast, the smooth PDMS surface reduced the dynamic

modulation of the conductive network, which lowered the piezoresistive sensitivity.

Supplementary Figure 6A and B presents the Raman and Fourier transform infrared (FTIR) spectra of the MWCNT/mPDMS system, respectively, which confirm that MWCNTs were successfully deposited on the surface of mPDMS. The elemental distribution of mPDMS is presented in Supplementary Figure 7A-C, wherein Si is shown to be dominant and C and O are present in relatively low proportions. These results are consistent with those of the energy spectrum characterization [Supplementary Figure 7D]. The elemental distribution of MWCNT/mPDMS is presented in Figure 2E-G, and the corresponding spectral results are shown in Supplementary Figure 8. Here, the C and O contents are significantly greater than those of mPDMS, and the peak intensity of C is slightly increased, indicating the successful deposition of MWCNTs onto the mPDMS surface.

Performance characterization of the flexible sensing unit

A wireless microcontroller-based acquisition module was developed to enable real-time transmission of the sensing signals [Supplementary Figures 9 and 10]. The performance of the flexible array was first characterized at the unit level. Calibration results from five fabrication batches exhibited exceptional uniformity, yielding a mean sensitivity of 1.364 kPa^{-1} and excellent linearity within 0-100 kPa [Figure 3A and B]. This near-linear response is attributed to the progressive contact evolution of the microstructured surface and the continuous modulation of the MWCNT conductive network. The working principle of the sensor is illustrated in Figure 3C, where the surface microstructure enables gradual contact modulation under zero-, low-, and high-pressure conditions, resulting in increased conductive pathways and corresponding electrical signal variations. The relative sensitivity deviation across batches was as low as 2.17%, while the calibrated linearity and repeatability errors remained below 2.6% and 1.3%, respectively [Supplementary Figure 11]. These results confirm the high reproducibility of the preparation process and provide a solid basis for manufacturable large-scale integration. Compared with representative thin-film pressure sensors reported in recent years [Supplementary Table 1], both wide-range detection and high sensitivity were achieved, overcoming the traditional tradeoff between compliance and measurement precision.

The high sensitivity is attributed to the hierarchical microstructured surface of the MWCNT/mPDMS composite. At low pressures, limited contact between the electrode and concave microstructures results in low baseline conduction; as pressure increases, the progressive contact growth reduces the tunneling resistance, resulting in an exponential-to-linear transition. Once the microstructures are fully compressed, further loading leads to a saturated response, forming a quasilinear region for calibration. This mechanism accounts for the excellent sensing precision and stability. The I–V curves display highly linear behavior [Figure 3D] and minimal frequency dependence [Figure 3E], while the cyclic loading tests show reproducible amplitudes with a hysteresis error of only 4.75% F.S. [Figure 3F and G]. The combination of low hysteresis and a high signal-to-noise ratio ensures accurate dynamic transduction for continuous handwriting recognition.

In addition to high sensitivity, the device exhibited a fast dynamic response, environmental resilience, and mechanical durability, all of which are essential yet rarely co-realized in soft-matter sensors. The unit detected pressures as small as 9.74 Pa and exhibited rapid response and recovery times of 12 and 16 ms, respectively [Figure 3H and I]. The sensor response was systematically evaluated under representative temperature conditions (20-45 °C) and bending angles (0°-50°) [Supplementary Figure 12]. The results show minimal signal fluctuation during real-time environmental changes and mechanical deformation, indicating good environmental and structural robustness. After 7 d of water immersion, the signal deviation was maintained below 1.02%, demonstrating the effectiveness of PDMS encapsulation in waterproofing and sweat resistance [Figure 3J and Supplementary Figure 13]. Under 45° cyclic bending at 2 Hz, the response

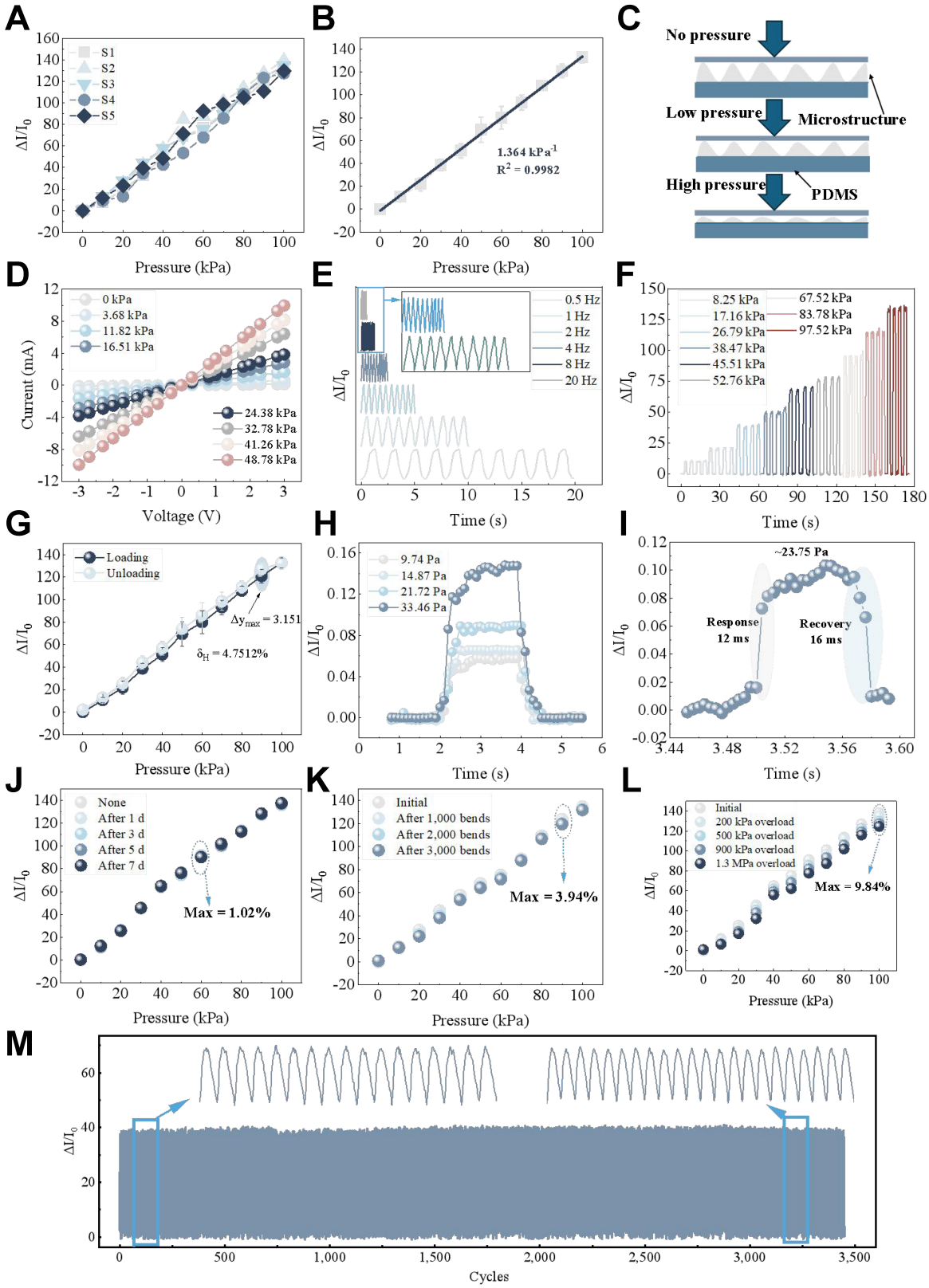

Figure 3. Performance characterization of the flexible sensing unit. (A) Calibration curves of different batches of sensors; (B) Sensitivity characterization. The error bars represent the SD of five batches of sensors; (C) Sensor operation principle; (D) I–V characteristic curves of the sensors; (E) Response curves for different frequencies at 20 kPa; (F) Response curves for four loading cycles at different pressures; (G) Full-scale hysteresis error. The error bars indicate the SDs obtained from repeated tests (n = 5); (H) Minimum resolving power; (I) Response and recovery time; (J) Waterproofing characteristics; (K) Bending resistance characteristics; (L) Overload stability; (M) Durability. SD: Standard deviation; PDMS: polydimethylsiloxane.

deviation remained within 3.94% [Figure 3K and Supplementary Figure 14], and after applying an overload of 1.3 MPa, the sensitivity was reduced by only 9.84% without significant deterioration in linearity or repeatability [Figure 3L, Supplementary Figures 15 and 16]. Long-term cyclic tests further demonstrated the mechanical endurance of this system, which exhibited a consistent response amplitude and a total deviation of approximately 6.3% after 3,000 loading cycles at 30 kPa [Figure 3M and Supplementary Figure 17]. Importantly, no drift in the baseline or sensitivity was observed, underscoring the excellent fatigue resistance of the MWCNT/mPDMS interface. The plasma-induced surface activation was found to improve the adhesion of the MWCNT network to PDMS, thereby contributing to its stable electrical response under repeated mechanical deformation cycles. Compared with previously reported devices, which often prioritized single metrics (e.g., sensitivity–range tradeoff or short-term response), multifactorial optimization was achieved, including ultrahigh sensitivity, broad detection range, rapid response dynamics, waterproof reliability, and long-term mechanical stability in a unified architecture. Moreover, the coupling between the hierarchical microstructure, conductive percolation, and elastomeric compliance enhanced signal fidelity and ensured stable performance under diverse operating conditions. This synergistic design principle allows for the precise spatiotemporal mapping of subtle muscle deformations, providing a robust foundation for array-level FMG sensing and high-accuracy handwriting decoding.

Flexible-sensing-array performance characterization

The sensitivity of the nine channels of the sensor array is presented in Supplementary Figure 18A and B, and an average value of 1.385 kPa^{-1} was obtained. The sensitivity of the nine channels relative to the average value [Supplementary Figure 18C] showed a maximum deviation of approximately 5.97%, indicating that the different channels demonstrate high consistency. The response curves of each channel of the flexible sensing array to a single-point external force are presented in Figure 4A. Clear responses to varying applied forces are shown, which enabled the differentiation of the location and magnitude of the applied force [Figure 4B-D]. The crosstalk of the flexible sensing array was calculated [Figure 4E-G], and the maximum crosstalk of the remaining channels was 4.34%, 4.58%, and 2.75% when only channels 1, 5, and 8 were subjected to an external force [Supplementary Note 2]. The crosstalk of each channel remained within a reasonable range under single-point loading, ensuring the measurement accuracy of the flexible sensing array. The flexible sensing array also demonstrated an effective mapping capability for multipoint forces, as illustrated by the response schematics and curves for objects of different shapes [Supplementary Figure 19A-D]. The calculated response heatmaps of the array are shown in Supplementary Figure 19E-G, wherein the flexible sensing array exhibited a reliable mapping performance for multipoint force distributions.

Hand-motion detection with flexible sensing arrays

To evaluate the performance of the wearable flexible sensing array, 10 healthy volunteers (five males and five females aged 22 ± 2 years, with no history of neuromuscular disorders) were recruited to participate in gesture- and handwriting-recognition tests [Supplementary Note 3 and Supplementary Figure 20]. The 3 × 3 sensing array was conformally attached to the dorsal forearm using a polyurethane film to prevent displacement [Supplementary Figure 21A]. Each sensing channel was connected in series with a 5 kΩ resistor and sampled at 50 Hz via a wireless microcontroller module [Supplementary Figures 9 and 10]. The deformation of local muscles during finger or wrist motion altered the pressure at the skin–sensor interface, resulting in measurable voltage changes across the array. Furthermore, by combining experimental measurements of the proposed system with reported data from representative wearable interfaces, the system-level performance (including the latency and user calibration time) was evaluated, thereby enabling a comprehensive assessment of real-time applicability [Supplementary Figure 21B and C]. The recorded time-domain signals exhibited periodic fluctuations consistent with the voluntary motion frequency (< 3 Hz), as confirmed by the fast Fourier transform and short-time Fourier transform analyses [Figure 5A and B, Supplementary Figure 22]. After applying low- and high-pass filters at 3 Hz, the low-frequency

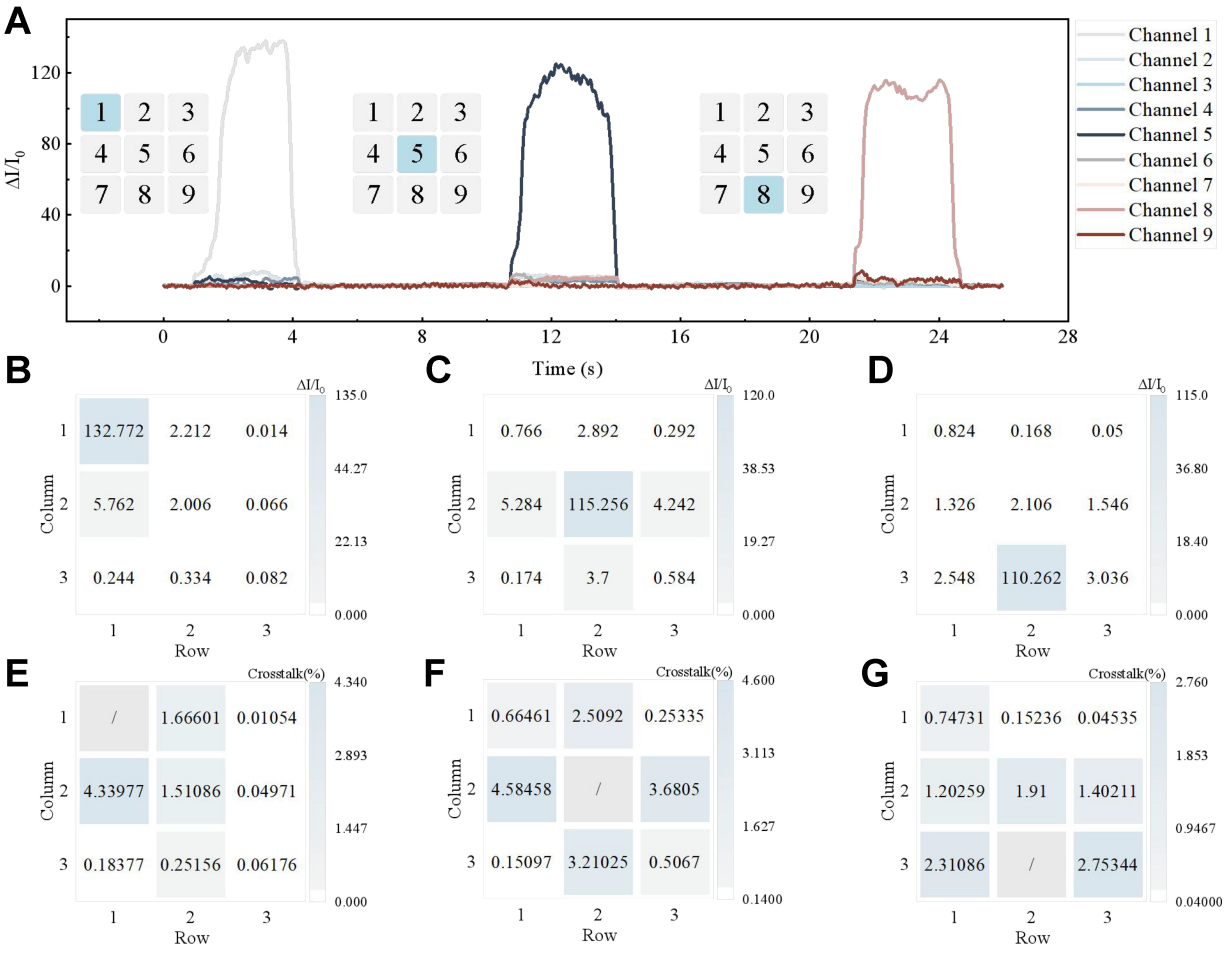

Figure 4. Characterization of the flexible sensing array. (A) Response curve for a single-point applied force; (B-D) Heat maps of the response to an applied force for channels 1, 5, and 8; (E-G) Heat maps of the crosstalk error for each channel when an external force was applied to channels 1, 5, and 8.

components reflected voluntary control, while the high-frequency residuals corresponded to intrinsic mechanomyographic signatures. The filtered signals retained distinct amplitude and phase patterns for different gestures [Figure 5A_2 and A_3], demonstrating the ability of the array to resolve muscle deformation dynamics at multiple temporal scales.

Each of the nine channels selectively responds to specific gestures, forming characteristic spatiotemporal response maps [Figure 5C and D]. Although certain channels exhibited partially similar patterns among hand gestures "0", "1", and "8", cross-channel comparison enables unambiguous classification. Repeated measurements showed highly consistent response timing and amplitude over 10 consecutive cycles [Figure 5E], confirming excellent repeatability. The corresponding power spectral density (PSD) maps further distinguish different gestures based on their spectral energy distribution [Figure 5F and G, Supplementary Figure 23]. Dimensionality reduction through principal component analysis and t-distributed stochastic neighbor embedding revealed compact clustering within identical gesture classes and clear separation between distinct gestures [Figure 5H].

Statistical evaluation of the root-mean-square (RMS) values and signal standard deviations (SDs) [Figure 5I and J, Supplementary Figures 24 and 25] showed that the motion states exhibited larger variance than the stationary states, confirming robust channel activation and effective noise suppression. Collectively, these

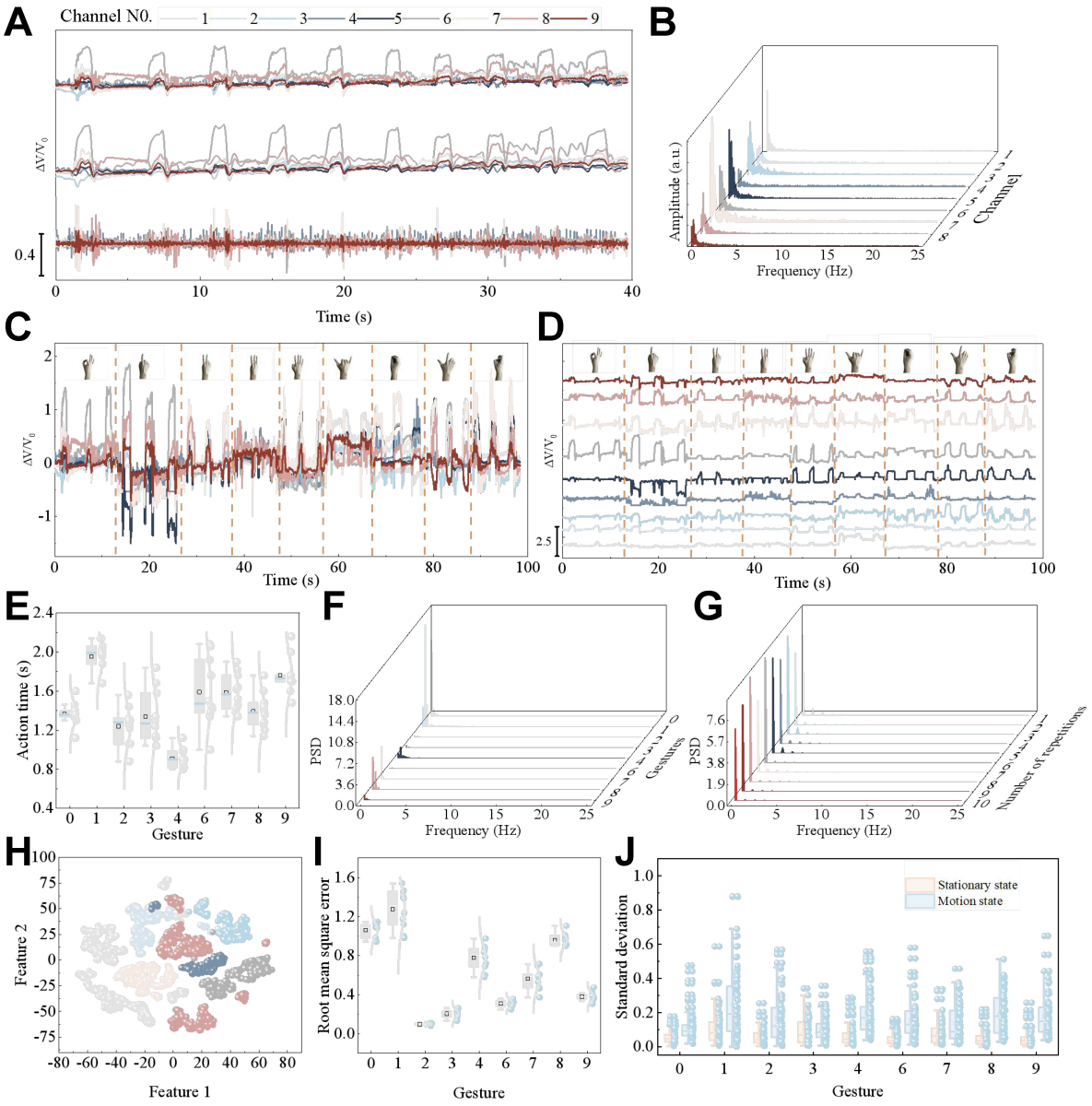

Figure 5. Response of the flexible sensing array to different hand motions. (A_1) Raw signal of 10 repetition cycles of hand movement "0", (A_2) 3 Hz low-pass-filtered signal of 10 repetition cycles of hand movement "0", (A_3) fast-pass filtered signal of hand movement "0" for 10 repetition cycles using a 3 Hz high-pass filtered signal; (B) Fast Fourier transform (a.u., arbitrary units) of the hand movement "0" signal; (C and D) three repetition cycles of the original signals of different hand movements; (E) Response times of different hand movements; (F) PSD curves from channel 6 for the nine different motions; (G) PSD curves for 10 repetition cycles of hand motion "0" for channel 6; (H) Mapping of different hand motion features in the 2D plane; (I) RMS of channel 6 for the detection of different hand motions; (J) SD of the rate of change of the output signals for the steady-state and motion states of the nine different hand motions. PSD: Power spectral density; RMS: root-mean-square; SD: standard deviation.

analyses demonstrate that the array captured muscular deformation with a high temporal resolution and specificity, thereby forming a stable biomechanical signature for each gesture.

To quantify recognition performance, a deep neural network (DNN) comprising three hidden layers (50–30–20 neurons) was trained on the acquired dataset, with an 80%/20% training/testing split [Figure 6A and Supplementary Note 4]. The recognition accuracy increased with the number of active channels, reaching 84.3%, 90.4%, 95.2%, 97.4%, and 99.6% for three-, four-, five-, six-, and nine-channel configurations,

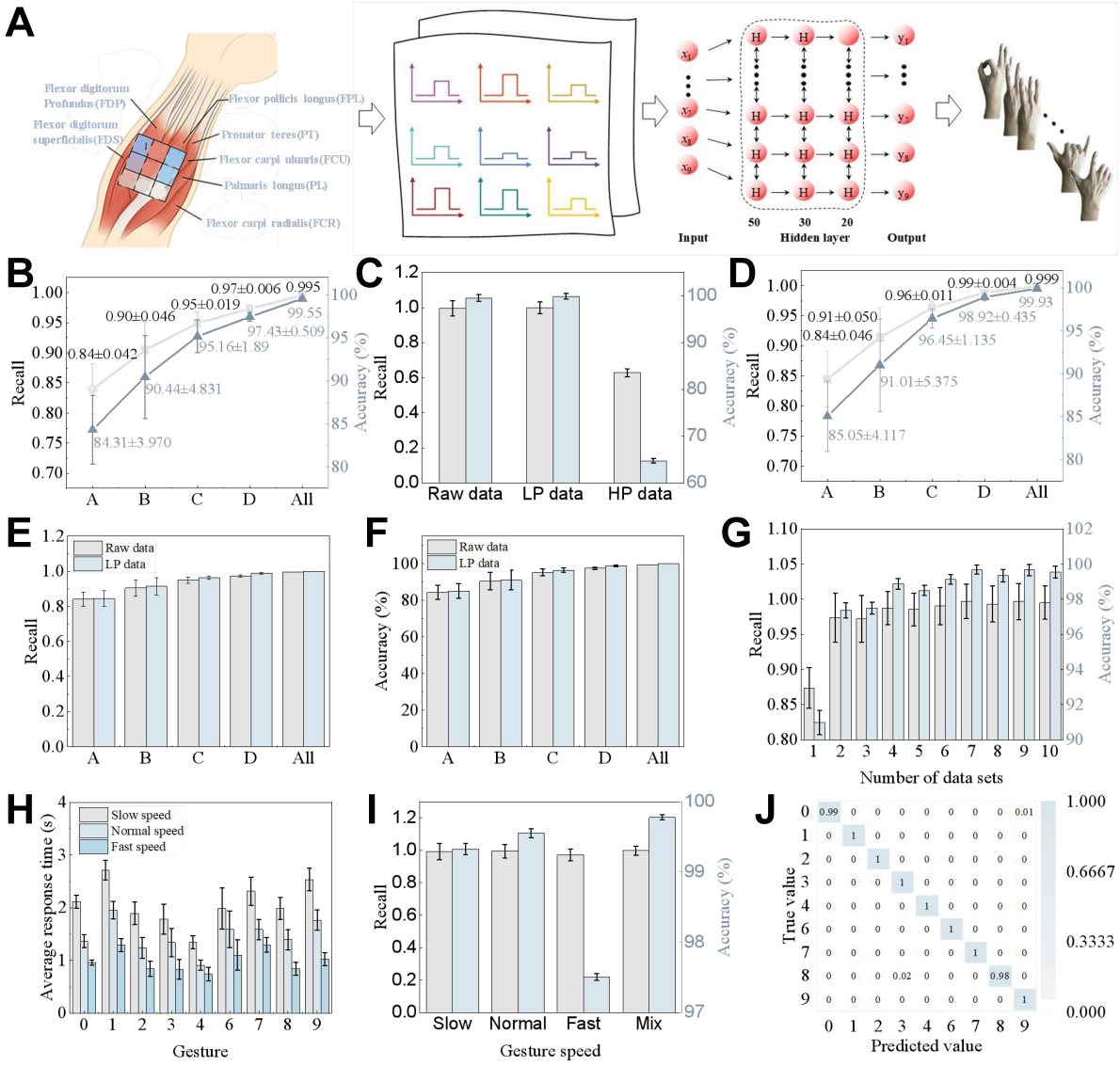

Figure 6. (A) Schematic of the DNN; (B) Recall and accuracy of classification prediction using raw data with different numbers of channels; (C) Recall and accuracy of predictions using high-pass-filtered data (HP data), low-pass-filtered data (LP data), and raw data; (D) Recall and accuracy of classification predictions using low-pass-filtered (< 3 Hz) data with different numbers of channels; (E) Recall and (F) accuracy of predictions using low-pass-filtered (< 3 Hz) data with different numbers of channels; (G) Recall and accuracy of predictions for each hand movement; (H) Average response time for different hand-movement speeds; (I) Recall and accuracy of predictions using different hand-movement speeds; (J) Confusion matrix for predictions made with mixed data. The error bars represent the SD obtained from a five-fold cross-validation. DNN: Deep neural network; SD: standard deviation.

respectively [Supplementary Figure 26 and Figure 6B]. Even when reduced to a four- or five-channel array, accuracies above 90% and 95% were obtained, respectively, suggesting that high recognition reliability can be achieved with fewer sensing sites. Channel arrangement had a negligible influence on recall and precision [Supplementary Figure 27]. By contrast, signal preprocessing affected classification outcomes, as high-pass-filtered data yielded poor prediction accuracy due to low signal amplitude and environmental noise, whereas low-pass-filtered data achieved comparable or slightly superior accuracy compared with raw data [Figure 6C-F and Supplementary Figure 28]. The effect of dataset size was further investigated by varying the number of motion repetitions. The recognition accuracy significantly improved from one to two repetitions but plateaued thereafter [Figure 6G, Supplementary Figures 29 and 30], indicating that high performance can be maintained with reduced data volume and computational cost.

The gesture recognition robustness was examined across different movement speeds [Figure 6H]. Extremely fast gestures resulted in reduced accuracy, while the inclusion of multispeed data during training restored and further enhanced the overall performance [Figure 6I and J, Supplementary Figure 31]. These results demonstrate the adaptability of the DNN model to intrasubject speed variations and its potential for generalized motion decoding.

Overall, the wearable array exhibited precise, repeatable, and high-fidelity detection of muscular deformation during voluntary motion. By coupling dense spatiotemporal sensing with machine-learning-based decoding, near-perfect gesture recognition (≈ 99.5%) was achieved without recalibration, establishing a scalable strategy for noninvasive human–machine interaction and neuromuscular monitoring.

Handwriting recognition using the flexible sensing arrays

As significant differences in hand-force generation are encountered when writing different symbols and words, the proposed flexible sensing array may be applied to the recognition and correction of handwriting. Figure 7A shows a schematic of the writing process, while Figure 7B presents the corresponding symbols and their stroke orders, such as counterclockwise and orthogonal circular motions. Letters, numbers, and Chinese characters with different stroke orders and continuous strokes were used to evaluate the performance of the proposed system [Figure 7C-E and Supplementary Figure 32]. Figure 7F shows the response curves of each channel when writing different shapes, demonstrating clear distinctions among shapes. The action time required for writing different shapes is presented in Figure 7G, which indicates that both shape and stroke sequence produced distinguishable temporal features for symbol identification. The RMS results obtained for channel 6 when different writing shapes are shown in Figure 7H, wherein clustered distributions for identical shapes and a clear separation between different shapes are observed. These results indicate that the proposed flexible sensing array effectively distinguishes different writing symbols and different writing sequences of the same symbol. The response curves generated during the writing of different characters are presented in Figures 7I and J, which demonstrate distinct multichannel signal patterns corresponding to different handwriting tasks.

As pen diameter and weight vary in practical applications, the effects of these parameters were investigated considering the writing-recognition accuracy. The flexible sensing array exhibited good response as the mass of the gripped object was varied [Supplementary Figure 33]. Here, a single pen was weighted using a tennis-racket weight to simulate different pen masses. The recognition performance obtained under different pen weights was further evaluated [Supplementary Figure 34 and Figure 7K]. The classification accuracies for the normal pen, slightly heavier pen, and heavier pen were 98.25% ± 1.47%, 97.93% ± 1.76%, and 98.37% ± 1.70%, respectively. Statistical analysis using a paired t-test showed no significant difference between these conditions ($P > 0.05$), indicating that the proposed FMG-based recognition system was robust toward variations in pen weight. By contrast, the responses of each channel when holding objects with different diameters significantly differed [Supplementary Figures 35 and 36]. The confusion matrix for symbol classification using pens of different thicknesses, achieved by wrapping the pen with tennis grip tape, is shown in Supplementary Figure 37, while the recall and classification accuracy for each pattern are presented in Figure 7L. Although the classification accuracy slightly decreased (from 98.13% to 97.25%) as the pen became thicker, the overall prediction accuracy remained high.

The action times of the written words are presented in Supplementary Figure 38, and the RMS of channel 6 is shown in Supplementary Figure 39. The action times and RMS significantly varied across different words, while variations within identical actions remain small. The classification confusion matrix for writing different words is shown in Supplementary Figure 40, and the recall and accuracy are provided in Supplementary Figure 41, demonstrating a high recognition accuracy of 96.35% ± 0.53%. Effective

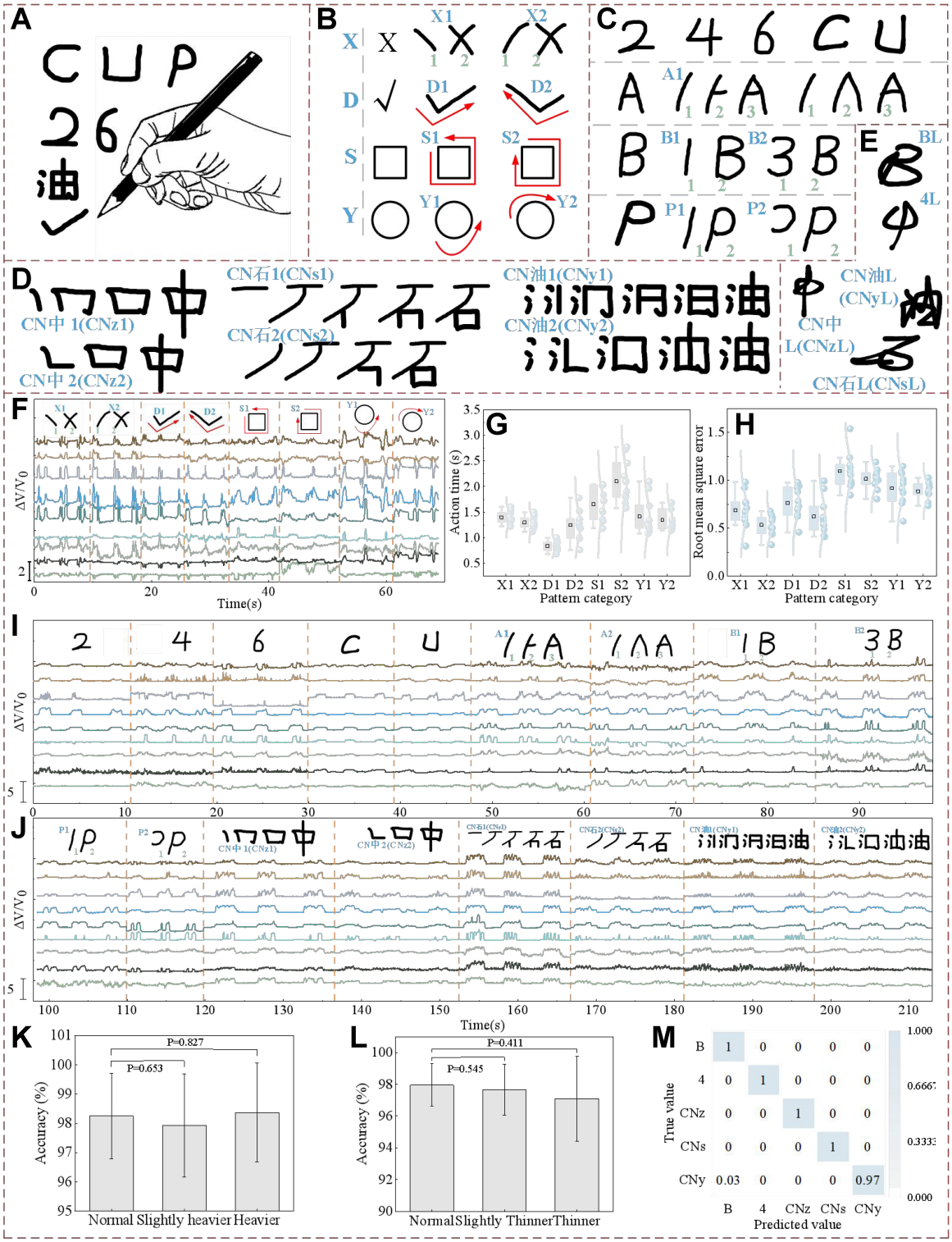

Figure 7. Writing-recognition results. (A) Schematic showing the writing of different words; (B) Writing symbols in different stroke orders; (C) Writing different numbers and letters; (D) Writing Chinese characters using different stroke orders; (E) Writing numbers, letters, and Chinese characters using a continuous stroke. Here, "中", "石", and "油" are Chinese characters, abbreviated as "CNz", "CNs", and "CNy", respectively. The numbers "1" and "2" represent different writing orders, and "L" represents cursive writing; (F) Response curves of each channel for symbols written using different stroke orders; (G) Action time for writing symbols using different stroke orders; (H) RMS for writing symbols using different stroke orders; (I and J) Response curves of each channel for writing numbers, letters, and Chinese characters using different stroke orders; Recognition accuracy of different characters under different pen (K) weight and (L) thickness conditions. The error bars represent the SD obtained from a five-fold cross-validation (n = 5). Data are presented as mean ± SD. Statistical analysis was performed using MATLAB R2023b (MathWorks, Natick, MA, USA). Paired t-tests were conducted based on matched cross-validation folds; (M) Confusion matrices for classifying different words during writing. RMS: Root-mean-square; SD: standard deviation.

differentiation was also achieved for different downstroke orders for the same word. Moreover, variances across shapes and stroke sequences enabled the effective discrimination between different writing symbols. The RMS value of the signal detected by channel 6 differed significantly across writing shapes, exhibiting clustered distributions for identical shapes and clear separation between different shapes. These results indicate that the proposed flexible sensing array effectively distinguishes different writing symbols and different writing sequences of the same symbol. To assess scalability, a 26-letter handwriting dataset was collected under natural writing conditions. The model achieved an accuracy of ~98.8% with errors mainly occurring among structurally similar letters, indicating strong discrimination under an expanded vocabulary [Supplementary Figure 42].

We further explored the impact of cursive writing on recognition accuracy. As shown in Supplementary Figures 43 and 44, the overall recognition accuracy reached 97.83% ± 0.22% and was unaffected by cursive writing. The confusion matrix and recall rate of different character classifications for datasets composed of mixed stroke orders and cursive variations of standard writing (for example, B includes B1, B2, and BL) are shown in Figure 7M and Supplementary Figure 45. An accuracy of 99.54% ± 0.16% was obtained when using mixed data for the classification and prediction of handwritten characters, which is significantly higher than that obtained using a single dataset ($P < 0.05$). Therefore, when constructing a dataset of written characters, the inclusion of different stroke orders and cursive writing methods is necessary to improve prediction accuracy. To evaluate the performance of different machine-learning models in the handwriting recognition task, four models [DNN, gated recurrent unit (GRU), long short-term memory (LSTM), and Transformer] were compared [Supplementary Table 2 and Supplementary Figure 46]. Among them, GRU, LSTM, and Transformer represent temporal modeling approaches capable of capturing time-dependent features in FMG signals, whereas DNN relies on multichannel instantaneous features for classification. All models achieved accuracies of > 99%, with Transformer achieving the highest accuracy and DNN achieving a comparable accuracy. Notably, DNN exhibited the smallest number of parameters, lowest model size, and fastest inference speed. Considering both the recognition performance and computational efficiency, the DNN model was selected for further investigation considering real-time and lightweight wearable applications.

Ablation studies were performed on network depth and regularization to validate the selected DNN model [Supplementary Tables 3 and 4]. Increasing the network depth improved feature representation, and an optimal performance was achieved using a three-layer architecture. Batch normalization and dropout both enhanced stability and generalization, and their removal resulted in performance degradation. To further assess model effectiveness, DNN, one-dimensional convolutional neural network (1D-CNN), LSTM, and an ensemble model were compared under the same protocol [Supplementary Figure 47]. DNN achieved the best overall performance, offering the highest accuracy despite having a slightly higher relative RMS error (RRMSE), and it was therefore selected for further handwriting recognition evaluation. This system also showed strong robustness in cross-subject evaluations. A leave-one-subject-out validation showed that the recognition accuracy remained above 97%. In addition, signal drift induced by repeated reattachment (10 cycles) remained below 1.6%, confirming the reliability of the system for practical wearable applications [Supplementary Note 5 and Supplementary Figure 48]. To evaluate robustness under dynamic motion, tests were conducted using different walking speeds. The model maintained a high accuracy under both slow (98.74% ± 0.37%) and fast (98.63% ± 0.42%) walking, with no significant difference compared with the baseline (99.54% ± 0.16%) [Supplementary Figure 49].

In addition, cross-age validation was performed using data from two participants that were over 40 years old. Without retraining on this group, the model achieved accuracies of 98.63% ± 0.42% and 98.71% ± 0.38%, with no significant difference compared with the baseline ($P = 0.067$ and 0.074; Supplementary Figure 50), demonstrating a strong generalization capability. To further assess robustness under a cognitive load, a

dual-task experiment was conducted in which participants performed continuous subtraction during handwriting. The system maintained a high accuracy of 97.65% ± 0.34% (P = 0.068; Supplementary Figure 51), indicating a stable decoding performance under attention fluctuation. Cross-continuity generalization experiments were conducted to evaluate the robustness of the model under different handwriting styles [Supplementary Figure 52]. When the training and testing styles were inconsistent, the recognition accuracy slightly decreased to 96.5% ± 0.21% (Normal → Legato) and 96.0% ± 0.17% (Legato → Normal). After introducing mixed handwriting samples for training, the accuracy significantly improved to 98.5% ± 0.13% (Mixed → Legato) and 99.09% ± 0.09% (Mixed → Normal), demonstrating enhanced cross-style generalization ability. To evaluate temporal robustness, time-sequential cross-validation was performed by training the model using early writing samples and testing it on later samples within the same session [Supplementary Figure 53]. The recognition accuracy was 99.34% ± 0.15%, with no significant difference compared with the Early → Early condition (99.54% ± 0.16%, P = 0.071). The analyzed system also maintained robust handwriting recognition across different writing modalities and scales. The recognition accuracy remained above 97% even for cursive and high-speed writing, with a < 1.5% deviation from discrete characters. Moreover, it exhibited minimal dependence on handwriting size (5-25 mm), confirming the geometric and temporal adaptability of the proposed FMG-based sensing array [Supplementary Note 6 and Supplementary Figure 54].

The findings of representative studies are listed in Supplementary Tables 5 and 6 to compare the proposed system with recently developed flexible-sensor gesture-recognition systems. The competitive advantages of our system are highlighted in terms of its accuracy and wearable-device integration. The proposed array uniquely integrates both gesture and stroke-order recognition tasks, demonstrating array-level reliability and handwriting capability beyond existing FMG or sEMG systems.

CONCLUSIONS

This study established a new paradigm for noninvasive handwriting perception by bridging high-fidelity mechanical sensing and intelligent neural decoding. The MWCNTs/mPDMS array achieved the simultaneous optimization of sensitivity, linearity, and durability, enabling the robust detection of tendon-driven microdeformations associated with complex handwriting dynamics. Through hybrid amplitude–frequency feature fusion, continuous, cursive, and style-variable handwriting was decoded by the neural network at near-perfect accuracy, exceeding conventional sEMG and FMG systems in cross-user stability and recognition accuracy. Mechanistic analysis confirmed a direct link between wrist flexor coordination and differential pressure signatures, validating the physiological interpretability of the signals. The real-time adaptability, fast recalibration, and mechanical endurance of the proposed system highlight its scalability for use in next-generation wearable interfaces, rehabilitation feedback systems, and digital neuromotor diagnostics.

Despite its high recognition accuracy, several limitations remain. First, the physiological interpretation of this system was derived from empirical correlations between handwriting motion and forearm pressure patterns, and this requires further validation using complementary techniques such as sEMG or ultrasound imaging. In addition, residual errors may influence feedback-driven motor learning, indicating that clinical applications require professional supervision and subject-specific calibration to ensure safety and reliability. Future work will focus on the evaluation of long-term stability under continuous wear, particularly emphasizing signal drift induced by sweat accumulation and skin–sensor interface variations. Moreover, clinical studies involving patients with motor impairments (e.g., stroke or Parkinson's disease) will be conducted to further explore the potential of this system in rehabilitation monitoring and functional assessment.

DECLARATIONS

Authors' contributions

Conceived and designed the study: Liu, L.; Xu, Y.; Jia, X.; Yao, J.
Led the overall research framework, performed the main data analysis, and interpreted the results: Liu, L.
Contributed to experimental design refinement and data analysis: Liu, H.; Li, S.; Zhou, H.
Responsible for data acquisition and assisted with experimental implementation: Wei, X.; Han, B.; Wang, D.
Provided funding acquisition and project administration, as well as overall supervision: Xu, Y.; Jia, X.
All authors discussed the results and contributed to the writing and revision of the manuscript.

Availability of code and data

The source code used for model training and data analysis has been made publicly available on GitHub (https://github.com/1169843834/Soft-Science). The dataset used in this study is available from the corresponding author upon reasonable request for academic research purposes only.

AI and AI-assisted tools statement

Not applicable.

Financial support and sponsorship

This work was supported by the National Natural Science Foundation of China (Grant No. 12372145), the Natural Science Foundation of Hebei Province (E2024203107), and the project "Key Components of Top Drive System for deep-Earth Oil and Gas Drilling and Exploration" (Grant No. TC240HAJ8-173).

Conflicts of interest

All authors declared that there are no conflicts of interest.

Ethical approval and consent to participate

This study involves noninvasive experiments that do not cause any physical or psychological harm to human participants; therefore, ethical approval is not required. All participants were fully informed about the purpose and procedures of the study prior to participation, and written informed consent was obtained from all individuals involved.

Consent for publication

Not applicable.

Supplementary Materials

Supplementary Materials

REFERENCES

1. Liu, L.; Jia, X.; Zhang, J.; et al. A high-sensitivity wearable flexible strain sensor based on three-dimensional twist-like network structure. *Proc. Inst. Mech. Eng. C.* **2024**, *238*, 2877-90. DOI
2. Chen, X.; Lin, X.; Mo, D.; et al. High-sensitivity, fast-response flexible pressure sensor for electronic skin using direct writing printing. *RSC. Adv.* **2020**, *10*, 26188-96. DOI PubMed PMC
3. Zhang, Y.; Zhang, B.; Lv, Y.; Wang, P.; Liu, T.; Meng, C. Flexible and breathable MXene-modified paper-based piezoresistive pressure sensors integrated into airbag pillow for sleep monitoring. *Soft. Sci.* **2025**, *5*, 17. DOI
4. Zhao, W.; He, P.; Ling, K.; et al. Printed graphene/CNTs/TPU-fabric wearable strain sensor for healthcare monitoring. *Soft. Sci.* **2025**, *5*, 10. DOI
5. Gao, Z.; Zhang, Q.; Wang, Y.; et al. 3D printing wide detection range and high sensitivity flexible pressure sensor and its applications. *React. Funct. Polym.* **2024**, *196*, 105840. DOI
6. Gu, M.; Zhao, B.; Gao, J.; et al. Nested-cell architecture and molecular surface modification enabled 10 megapascals range high sensitivity flexible pressure sensors for application in extreme environment. *Adv. Funct. Mater.* **2024**, *34*, 2400494. DOI

7. Guo, X.; Zhao, J.; Hu, B.; et al. Flexible pressure sensor with high sensitivity and fast response based on bionic honeycomb-structured polydimethylsiloxane/aluminum oxide composites dielectric via 3-D printing. *IEEE. Trans. Electron. Devices.* **2024**, *71*, 4283-91. DOI
8. Hong, W.; Guo, X.; Zhang, T.; et al. Flexible capacitive pressure sensor with high sensitivity and wide range based on a cheetah leg structure via 3D printing. *ACS. Appl. Mater. Interfaces.* **2023**, *15*, 46347-56. DOI PubMed
9. Hou, Y.; Wang, L.; Sun, R.; et al. Crack-across-pore enabled high-performance flexible pressure sensors for deep neural network enhanced sensing and human action recognition. *ACS. Nano.* **2022**, *16*, 8358-69. DOI PubMed
10. Kim, J.; Campbell, A. S.; de Ávila, B. E.; Wang, J. Wearable biosensors for healthcare monitoring. *Nat. Biotechnol.* **2019**, *37*, 389-406. DOI PubMed PMC
11. Kireev, D.; Sel, K.; Ibrahim, B.; et al. Continuous cuffless monitoring of arterial blood pressure via graphene bioimpedance tattoos. *Nat. Nanotechnol.* **2022**, *17*, 864-70. DOI PubMed
12. Kong, K.; Wang, L.; Wu, H.; et al. Skin-inspired multimodal tactile sensor aiming at smart space extravehicular multi-finger operations. *Chem. Eng. J.* **2024**, *498*, 154870. DOI
13. Lee, J. H.; Cho, K.; Kim, J. K. Age of flexible electronics: emerging trends in soft multifunctional sensors. *Adv. Mater.* **2024**, *36*, e2310505. DOI PubMed
14. Li, S.; Yang, M.; Wu, Y.; et al. A flexible dual-mode sensor with decoupled strain and temperature sensing for smart robots. *Mater. Horiz.* **2024**, *11*, 6361-70. DOI PubMed
15. Lin, M.; Zhang, Z.; Gao, X.; et al. A fully integrated wearable ultrasound system to monitor deep tissues in moving subjects. *Nat. Biotechnol.* **2024**, *42*, 448-57. DOI PubMed
16. Liu, L.; Jia, X.; Yang, Q.; et al. Optimisation of properties of multidimensional hybrid polymer nanocomposites for flexible pressure sensors. *Chem. Eng. J.* **2024**, *493*, 152705. DOI
17. Liu, L.; Jia, X.; Yang, Q.; et al. Design and application of a new high-performance flexible six-axis force/torque sensor for massage therapy. *Measurement* **2025**, *243*, 116312. DOI
18. Liu, L.; Jia, X.; Zhang, J.; et al. Preparation and application of flexible pressure/strain sensors based on loofahs. *IEEE. Sens. J.* **2024**, *24*, 2608-19. DOI
19. Liu, X.; Li, K.; Qian, S.; et al. A high-sensitivity flexible bionic tentacle sensor for multidimensional force sensing and autonomous obstacle avoidance applications. *Microsyst. Nanoeng.* **2024**, *10*, 149. DOI PubMed PMC
20. Liu, X.; Ma, Y.; Dai, X.; Li, S.; Li, B.; Zhang, X. Flexible pressure sensor based on Pt/PI network with high sensitivity and high thermal resistance. *Chem. Eng. J.* **2024**, *494*, 152996. DOI
21. Luo, R.; Wu, J.; Dinh, N.; Chen, C. Gradient porous elastic hydrogels with shape-memory property and anisotropic responses for programmable locomotion. *Adv. Funct. Mater.* **2015**, *25*, 7272-9. DOI
22. Luo, Y.; Li, J.; Ding, Q.; Wang, H.; Liu, C.; Wu, J. Functionalized hydrogel-based wearable gas and humidity sensors. *Nanomicro. Lett.* **2023**, *15*, 136. DOI PubMed PMC
23. Luo, Y.; Liu, C.; Lee, Y. J.; et al. Adaptive tactile interaction transfer via digitally embroidered smart gloves. *Nat. Commun.* **2024**, *15*, 868. DOI PubMed PMC
24. Amjadi, M.; Kyung, K.; Park, I.; Sitti, M. Stretchable, skin-mountable, and wearable strain sensors and their potential applications: a review. *Adv. Funct. Mater.* **2016**, *26*, 1678-98. DOI
25. Meng, K.; Xiao, X.; Liu, Z.; et al. Kirigami-inspired pressure sensors for wearable dynamic cardiovascular monitoring. *Adv. Mater.* **2022**, *34*, e2202478. DOI PubMed
26. Meng, X.; Zhang, C.; Xie, H.; Niu, S.; Han, Z.; Ren, L. A continuous pressure positioning sensor with flexible multilayer structures based on a combinatorial bionic strategy. *Adv. Funct. Mater.* **2024**, *34*, 2314479. DOI
27. Yao, S.; Zhu, Y. Wearable multifunctional sensors using printed stretchable conductors made of silver nanowires. *Nanoscale* **2014**, *6*, 2345-52. DOI PubMed
28. Shen, H. Y.; Li, Y. T.; Liu, H.; et al. Machine learning-assisted gesture sensor made with graphene/carbon nanotubes for sign language recognition. *ACS. Appl. Mater. Interfaces.* **2024**, *16*, 52911-20. DOI PubMed
29. He, K.; Zhang, X.; Ren, S.; Sun, J. Deep residual learning for image recognition. In *2016 IEEE Conference on Computer Vision and Pattern Recognition (CVPR)*, Las Vegas, USA. June 27-30, 2016. IEEE; 2016. pp. 770-8. DOI
30. Suo, J.; Liu, Y.; Wang, J.; et al. AI-enabled soft sensing array for simultaneous detection of muscle deformation and mechanomyography for metaverse somatosensory interaction. *Adv. Sci.* **2024**, *11*, e2305025. DOI PubMed PMC
31. Xu, C., Lu, H., Liu, Z. Luo, N.; Wei, A. Flexible piezoresistive sensors based on porous PDMS/CB composite materials prepared by the solvothermal method. *J. Mater. Sci. Mater. Electron.* **2023**, *34*, 906. DOI
32. Wang, C.; Li, X.; Hu, H.; et al. Monitoring of the central blood pressure waveform via a conformal ultrasonic device. *Nat. Biomed. Eng.* **2018**, *2*, 687-95. DOI PubMed PMC

33. Park, S.; Heo, S. W.; Lee, W.; et al. Self-powered ultra-flexible electronics via nano-grating-patterned organic photovoltaics. *Nature* **2018**, *561*, 516-21. DOI PubMed
34. Wang, X.; Wu, G.; Zhang, X.; et al. Traditional Chinese Medicine (TCM)-inspired fully printed soft pressure sensor array with self-adaptive pressurization for highly reliable individualized long-term pulse diagnostics. *Adv. Mater.* **2025**, *37*, e2410312. DOI PubMed
35. Yu, H.; Jiang, S.; Zhan, W.; et al. Formaldehyde oxidation boosts ultra-low cell voltage industrial current density water electrolysis for dual hydrogen production. *Chem. Eng. J.* **2023**, *475*, 146210. DOI
36. Wu, Z.; Pan, H.; Huang, P.; Tang, J.; She, W. Biomimetic mechanical robust cement-resin composites with machine learning-assisted gradient hierarchical structures. *Adv. Mater.* **2024**, *36*, e2405183. DOI PubMed
37. Xu, L.; Zhang, Z.; Gao, F.; et al. Self-powered ultrasensitive pulse sensors for noninvasive multi-indicators cardiovascular monitoring. *Nano. Energy.* **2021**, *81*, 105614. DOI
38. Xu, T.; Song, Q.; Liu, K.; et al. Nanocellulose-assisted construction of multifunctional MXene-based aerogels with engineering biomimetic texture for pressure sensor and compressible electrode. *Nanomicro. Lett.* **2023**, *15*, 98. DOI PubMed PMC
39. Zhan, L.; Lv, J.; Chen, S.; et al. Moisture-triggered hybrid soft actuator and electric generator for self-sensing wearables and adaptive human-environment interaction. *Nano. Energy.* **2024**, *132*, 110410. DOI
40. Trung, T. Q.; Lee, N. E. Flexible and stretchable physical sensor integrated platforms for wearable human-activity monitoringand personal healthcare. *Adv. Mater.* **2016**, *28*, 4338-72. DOI PubMed
41. Zhao, H.; Zhang, Y.; Han, L.; et al. Intelligent recognition using ultralight multifunctional nano-layered carbon aerogel sensors with human-like tactile perception. *Nanomicro. Lett.* **2023**, *16*, 11. DOI PubMed PMC
42. Zhang, P.; Zhang, X.; Teng, M.; et al. Leather-based shoe soles for real-time gait recognition and automatic remote assistance using machine learning. *ACS. Appl. Mater. Interfaces.* **2024**, *16*, 62803-16. DOI PubMed
43. Zhao, Z.; Guo, Q.; Sun, Y.; et al. Bioinspired hierarchical structure for an ultrawide-range multifunctional flexible sensor using porous expandable polyethylene/loofah-like polyurethane sponge material. *Adv. Intell. Syst.* **2023**, *5*, 2200295. DOI
44. Zhou, H.; Gui, Y.; Gu, G.; et al. A plantar pressure detection and gait analysis system based on flexible triboelectric pressure sensor array and deep learning. *Small* **2025**, *21*, e2405064. DOI PubMed
45. Zhu, J.; Song, Y.; Xue, X.; Liu, Z.; Mao, Q.; Jia, Z. An eco-friendly and highly sensitive loofah@CF/CNT 3D piezoresistive sensor for human activity monitoring and mechanical cotrol. *Sci. China. Technol. Sci.* **2022**, *65*, 2667-74. DOI
46. Zhang, S.; Feng, W.; Jiang, Y.; et al. Flexible pressure sensor based on 3D printing MXene@dual-scale porous polymer. *Chem. Eng. J.* **2024**, *498*, 155356. DOI
47. Si, S.; Sun, C.; Wu, Y.; et al. 3D interlocked all-textile structured triboelectric pressure sensor for accurately measuring epidermal pulse waves in amphibious environments. *Nano. Res.* **2024**, *17*, 1923-32. DOI
48. Meng, K.; Chen, J.; Li, X.; et al. Flexible weaving constructed self-powered pressure sensor enabling continuous diagnosis of cardiovascular disease and measurement of cuffless blood pressure. *Adv. Funct. Mater.* **2019**, *29*, 1806388. DOI
49. Wang, J.; Zhu, Y.; Wu, Z.; et al. Wearable multichannel pulse condition monitoring system based on flexible pressure sensor arrays. *Microsyst. Nanoeng.* **2022**, *8*, 16. DOI PubMed PMC
50. Ren, Y.; Liu, Z.; Jin, G.; et al. Electric-field-induced gradient ionogels for highly sensitive, broad-range-response, and freeze/heat-resistant ionic fingers. *Adv. Mater.* **2021**, *33*, e2008486. DOI PubMed